Surfaces and Interfaces 34 (2022) 102396

Contents lists available at ScienceDirect

Surfaces and Interfaces

journal homepage: www.sciencedirect.com/journal/surfaces-and-interfaces

Thermoelectric properties and the effect of biaxial strain and external electric fields on the electronics of novel 2D Lace-like O-Pd_2Q_3 (Q= S, Se) monolayers

Dhara Raval [a], Elie A. Moujaes [b], Sanjeev K. Gupta [c,*], P.N. Gajjar [a,*]

[a] Department of Physics, University School of Sciences, Gujarat University, Ahmedabad, Gujarat 380009, India
[b] Physics Department, Federal University of Rondônia, Porto Velho 76801-974, Brazil
[c] Computational Materials and Nanoscience Group, Department of Physics and Electronics, St. Xavier's College, Ahmedabad 380009, India

ARTICLE INFO

Keywords:
O-Pd2Q3 monolayer
Carrier mobility
External electric field
Biaxial strain
Thermoelectric properties

ABSTRACT

Inspired by the experimental synthesis of the novel 2D O-Pd_2Se_3 monolayer, we performed density functional theory calculations to reveal detailed investigations of the electronics, and thermal properties of 2D O-Pd_2Q_3 (Q= S, Se) monolayers. The O-Pd_2S_3 and Pd_2Se_3 are semiconductors with indirect band gaps of 0.43 eV and 0.33 eV, respectively. Through strain engineering, the bulk modulus B (N/m) and young's modulus Y (N/m) are also determined to acquire a deep understanding of the elasticity of the monolayers. We find that the bandgaps tend to increase with increasing tensile biaxial strain (+ε%), and decrease with increasing compressive biaxial strain (-ε%). In particular, the O-Pd_2Se_3 monolayer starts to manifest a metallic feature at -5%. More importantly, we note that at room temperature, and under biaxial strain, O-Pd_2S_3 (O-Pd_2Se_3) has a high electron (hole) carrier mobility up to ~ 766 $cm^2 V^{-1} s^{-1}$ (~ 106 $cm^2 V^{-1} s^{-1}$). We have also tuned the band gaps of the monolayers via the application of an external electric field, along the z-direction. We find that, in the [-2.5, +2.5] V/Å range, such external electric fields reduce the bandgaps in both monolayers, transforming Pd_2Se_3 into a metal at a strength of ± 2.5 V/Å. Additionally, we have perceived that the thermoelectric (TE) properties of these materials exhibit an anisotropic behavior at ambient and higher temperatures. At 300K, the O- Pd_2Se_3 monolayers show a large thermal electronic conductivity and a power factor of about 18 (16) times that of O-Pd_2S_3 along the x (y) directions. At temperatures higher than 600K, these properties become more dominant in O-Pd_2S_3. The acquired power factor of O-Pd_2S_3 (O-Pd_2Se_3) is much higher than that of the 1T phase of PdS_2 (1T $PdSe_2$ and penta-$PdSe_2$). By just knowing the group velocities of the three acoustical modes, we were able to determine the minimum lattice thermal conductivity, which is 0.207 W/(m.K) for both systems. If properly exploited, these characteristics make the O-Pd_2Q_3 monolayers excellent candidates for the fabrication of novel ultrathin electronic and TE nanodevices at ambient and higher temperatures.

1. Introduction

Graphene (2D) [1] has become one of the most sparkling stars in the field of 2D materials because of its outstanding properties, and its ability to break the long-held belief that 2D structures are not stable -and hence cannot exist in nature- due to thermodynamical instability. Noble-metal dichalcogenides (TMCs) including $PdSe_2$ [2,3], MoS_2 [4,5], WS_2 [6], $ReSe_2$ [7] and VS_2 [8] have attracted significant attention in the last few years, because of their great potentials in electronic and optical devices; these comprise high stability, high carrier mobility, large current on/off ratio field-effect transistors (FETs) [9], photodetectors [10,11], solar cell [12] and valleytronics [13] applications. Among them, the noble palladium-based dichalcogenides, PdS_2 and $PdSe_2$ [14–18] have brought special interest to fabricating nanodevices, owing to their 2D unique atomic configurations and structural novelty, thus enhancing the electronic, optical, and thermoelectrical performances of the materials. Although the bulk form of the Pd_2Se_3 compound is not yet reported, Lin et al., [19] successfully synthesized the 2D semiconducting O-Pd_2Se_3 by fusing a few layers of $PdSe_2$, and introducing Se vacancies from the few-layered $PdSe_2$ crystals, hereby decreasing the Se/Pd element ratio. Replacing S with Se in the O-Pd_2Se_3 monolayer can form the stable O-Pd_2S_3 monolayer and reveal its hidden in-plane properties [20,21].

* Corresponding author.
E-mail addresses: sanjeev.gupta@sxca.edu.in (S.K. Gupta), pngajjar@gujaratuniversity.ac.in (P.N. Gajjar).

https://doi.org/10.1016/j.surfin.2022.102396
Received 9 August 2022; Received in revised form 12 September 2022; Accepted 4 October 2022
Available online 10 October 2022

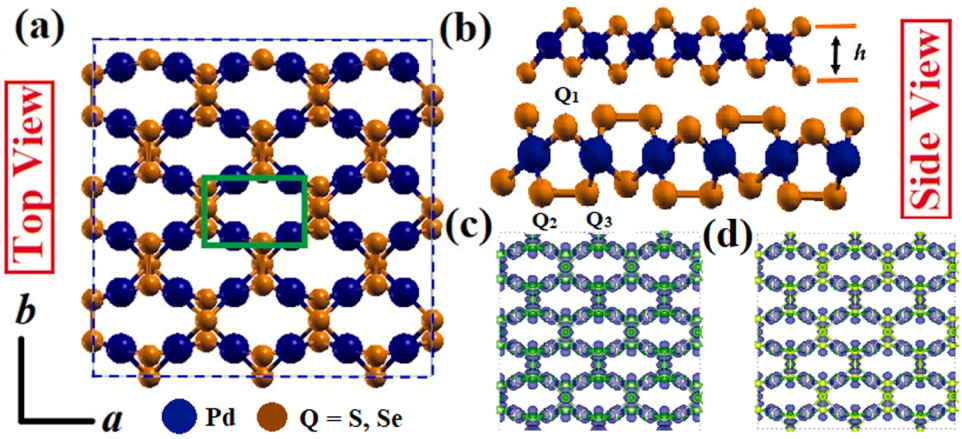

Fig. 1. (a) Top and (b) side views of the relaxed atomic structures of the O-Pd_2Q_3 (Q=S, Se) monolayers. The highlighted green box englobes the atoms in the unit cell. (c) The deformation charge density plot for O-Pd_2S_3; the blue color indicates charge accumulation (electron excess), and the green color a charge depletion (electron loss). (d) Same as (c) but for the O-Pd_2Se_3 monolayer. The iso-level is 0.07 e/Å^3 for both materials.

Subsequently, Naghavi et al., [22] has reported the thermoelectrical properties of the Pd_2Se_3 monolayer and showed that it is a highly efficient TE material in both n-type and p-type applications, due to the coexistence of different types of chemical bonds, combined with a square-planar crystal field, and a high figure of merit (*ZT*). Li et al., [23] used density functional theory calculations to predict the physical and photovoltaic properties of the semiconducting Pd_2Se_3 monolayer; they reported that it is promising as an absorber for future ultrathin photovoltaic devices, because of the high electron mobility and the strong optical absorption in the visible solar spectrum. Furthermore, Xiong et al., [20] systematically examined the structural, mechanical, electronic, and optical characteristics of the H-MX_2, O-MX_2, and O-M_2X_3 (M= Pd, Ni; X= S, Se, Te) monolayers via a DFT approach. They concluded that the O-Ni_2Se_3 and O-Pd_2Se_3 could be flexible for water splitting photocatalyst applications, thanks to the suitable band edges, band gaps, and ultrahigh sunlight absorption. Recently, another work by Naghavi et al. [21] comprehensively studied the whole family of the Pd_2Q_3 (Q= S, Se, Te, O) compounds with first-principles calculations, and deduced that all structures are metastable, having superior optical properties that can classify them as the most favorable visible-light absorber materials.

Among all the previous research papers on O-Pd_2Q_3 monolayers, none has explored the influence of an external electric field on the band edges of the electronic band structures of O-Pd_2Q_3. Besides, despite the fact that the thermoelectric properties of the O-Pd_2Se_3 system have been reported [22], those of the O-Pd_2S_3 monolayer are still lacking. Likewise, none has reported the bi-axial carrier mobility of the O-Pd_2Q_3 monolayer. All of these reasons encouraged us to conduct research tackling these points in the O-Pd_2Q_3 monolayers. The rest of the manuscript is devised as follows: In section 2, the computational methods, as well as the transport and thermoelectric theories are detailed. Section 3 involves the results of our calculations with a subsequent discussion. More specifically, we have described the geometrical and electronic characteristics of the 2D O-Pd_2S_3 and Pd_2Se_3 systems in section 3.1. While section 3.2 discusses the transport properties in terms of the carrier mobility (μ_{2D}) under a biaxial strain ε, section 3.3 is dedicated to the effect of applying an external electric field on the electronic properties of both lace-like monolayers. The thermoelectric properties of both materials are examined in section 3.4. Finally, the most important findings are recapped in section 4.

2. Computational details and theory

The structural, electronic, and transport properties of 2D O-Pd_2Q_3 (Q = S, Se) monolayers were performed within the SIESTA code [24]. The Generalized gradient approximation (GGA) of the Perdew–Burke-Ernzerhof (PBE) pseudopotential was considered to treat the interaction between the ion cores and valence electrons [25]. The cut-off kinetic energy for the plane wave basis is set to 450 Ry and 300 Ry for O-Pd_2S_3 and O-Pd_2Se_3, respectively. To expand the Kohn-Sham (KS) orbitals, the doubled zeta plus (DZP) basis set was used, with smearing energy of 0.02 Ry, and a split-valence scheme was adopted for the multiple zeta function. To define the sensible radii, the split norm value was taken to be 0.150. The Brillouin zone was sampled by a Γ-centred 30 × 30 × 1 mesh for O-Pd_2S_3 and a 20 × 20 × 1 grid for O-Pd_2Se_3. The structures were relaxed until the force acting on the atoms reduces to 0.01 eV/Å. The phonon dispersion curves were determined using the density functional perturbation theory (DFPT) formalism [26]. The bulk modulus B (N/m) and Young's modulus Y (N/m) were evaluated via the expressions $B = A_0\frac{\partial^2 E}{\partial A^2}$ and $Y = \frac{1}{A}\frac{\partial^2 E}{\partial \varepsilon^2}$ where A refers to the deformed cross-sectional area, A_0 is that of the unstrained unit cell, and E is the total energy after deformation [3].

The carrier mobility can be obtained via the Bardeen-Shockley formula [27] as $\mu_{2D} = \frac{2e\hbar^3 C_{2D}}{3k_B T|m^*|^2 (E_1)^2}$. Here, e is the elementary charge of an electron, and ħ is the reduced Planck's constant. C_{2D}, the in-plane stiffness constant, is defined as $C_{2D} = \frac{1}{A_0}\frac{\partial^2 E}{\partial\left(\frac{a}{a_0}\right)^2}$, with a_0 being the equilibrium lattice constant, and a the new lattice constant of the monolayers after deformation. k_B is the Boltzmann constant, T is temperature, and m^* is the effective mass in the transport direction, given by $m^* = \hbar^2\left\{\frac{d^2E}{dk^2}\right\}^{-1}$, directly derived from the electronic band structures of the O-Pd_2Q_3 monolayers. E_1 refers to the deformation potential (DP) constant, which is just the shift of each band edge as a result of the applied biaxial strain; mathematically, it can be computed as $E_1 = \frac{\partial E_{edge}}{\partial\left(\frac{a}{a_0}\right)}$ with E_{edge} being the energy value of the valence band maxima (VBM) and the conduction band minima (CBM). The electronic lifetime (τ) can then be evaluated as $\tau = \frac{\mu_{2Dm^*}}{e}$.

To determine the thermoelectric performance of a material, it is vital to compute its thermoelectric properties, namely the Seebeck coefficient (S), the electronic conductivity (σ), and the thermal electronic (κ) and thermal lattice (κ_L) conductivities. The determination of κ_L at any temperature is beyond the scope of this research; however, towards the end of the manuscript, we will determine a value of κ_L within the high-temperature limit. For the time being, we will only focus on the first three quantities. From the Boltzmann transport theory [28,29], the tensor components {α,β≡ xx, yy, zz} of κ, σ, and S can be defined as:

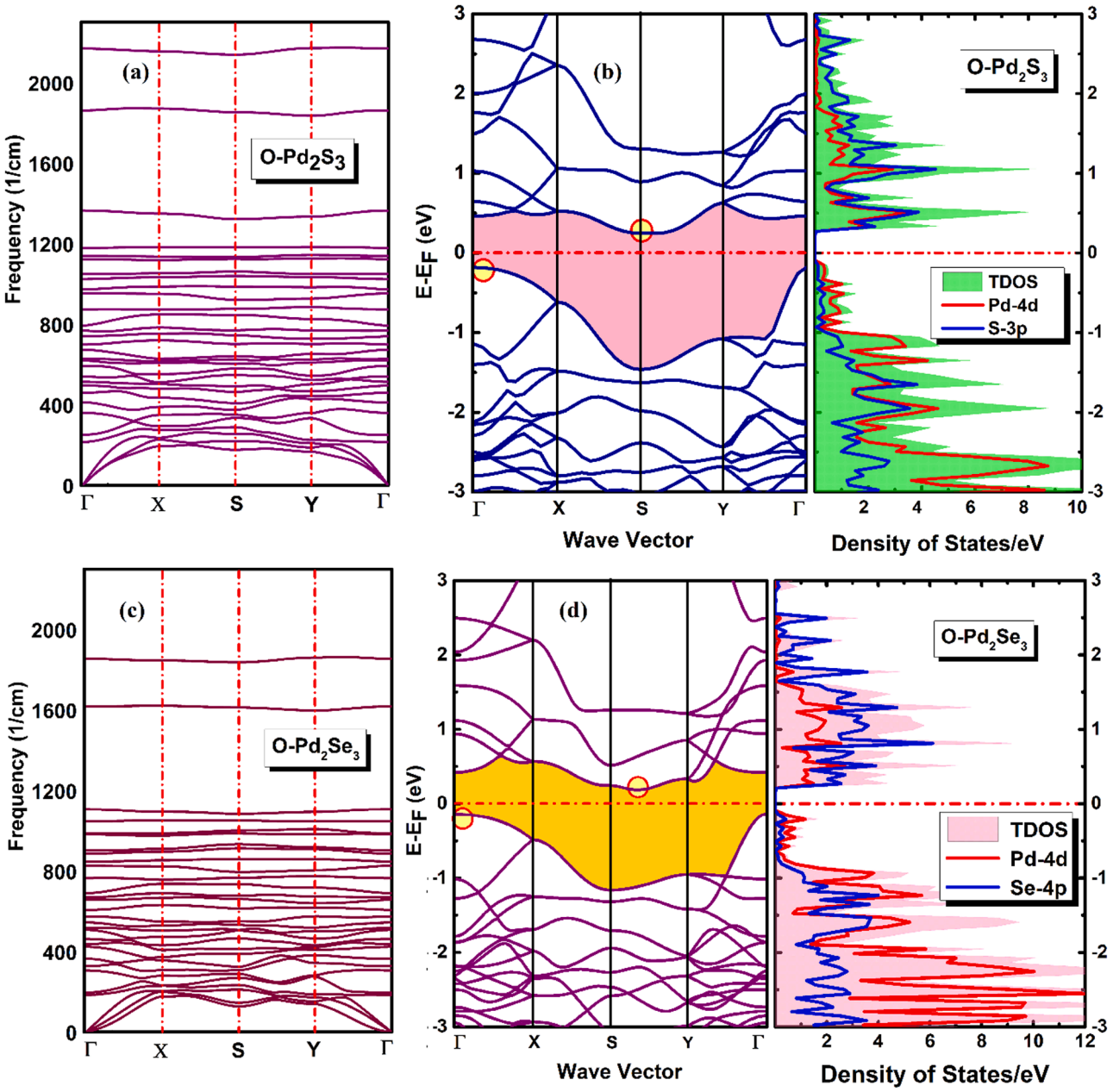

Fig. 2. Phonon dispersive curves of the O-Pd_2Q_3 monolayers (a, c). Calculated electronic band structures and density of states of (b) O-Pd_2S_3 and (d) O-Pd_2Se_3. The Fermi energy has been shifted to the zero level and is represented by a horizontal dashed red line. The red circles mark the VBM and CBM positions.

$$\kappa^{\alpha\beta}(E) = \sum_{n,k} \tau_{nk} v_g^{\alpha}(n,k) v_g^{\beta}(n,k) \delta(E - E_{nk}) \quad (1)$$

$$\sigma^{\alpha\beta}(T,\mu_c) = \frac{e^2}{NV} \int \sum_{n,k} \tau_{nk} v_g^{\alpha}(n,k) v_g^{\beta}(n,k) \delta(E - E_{nk}) \times \left[-\frac{\partial f(T,E,\mu_c)}{\partial E} \right] dE \quad (2)$$

$$S^{\alpha\beta}(T,\mu_c) = \frac{1}{eVT\sigma^{\alpha\beta}(T,\mu_c)} \int \sum_{n,k} \kappa^{\alpha\beta}(E - \mu_c) \times \left[-\frac{\partial f(T,E,\mu_c)}{\partial E} \right] dE. \quad (3)$$

N and V are the number of k points sampled, and the volume of the unit cell respectively. f is the famous Fermi-Dirac distribution function, μ_c (not to be confused with the mobility μ_{2D}) is the chemical potential. $v_g^{\alpha}(n,k)$, E_{nk} and τ_{nk} represent the α^{th} component of the group velocity of electrons (or holes), the electronic energy, and the electronic relaxation time of the n^{th} electronic band at the k^{th} point in the first Brillouin zone, respectively. It is important to note that in this work, we adopt the constant relaxation time approximation (RTA), which assumes that the electronic lifetime is both k-point and band independent; therefore, τ_{nk} can be set to a constant value τ, and can thus be taken out of the integral in the above expressions.

S, σ, and κ were computed using the BoltzWann code [30], which is implemented in the QE code [31]. It makes use of the Wannier functions [32] to construct the bands around the Fermi energy, necessary for the evaluation of the thermoelectric properties. 150 × 150 × 1 and 180 × 180 × 1 dense grids were sufficient to obtain converged results for the O-Pd_2S_3 and the O-Pd_2Se_3 monolayers respectively.

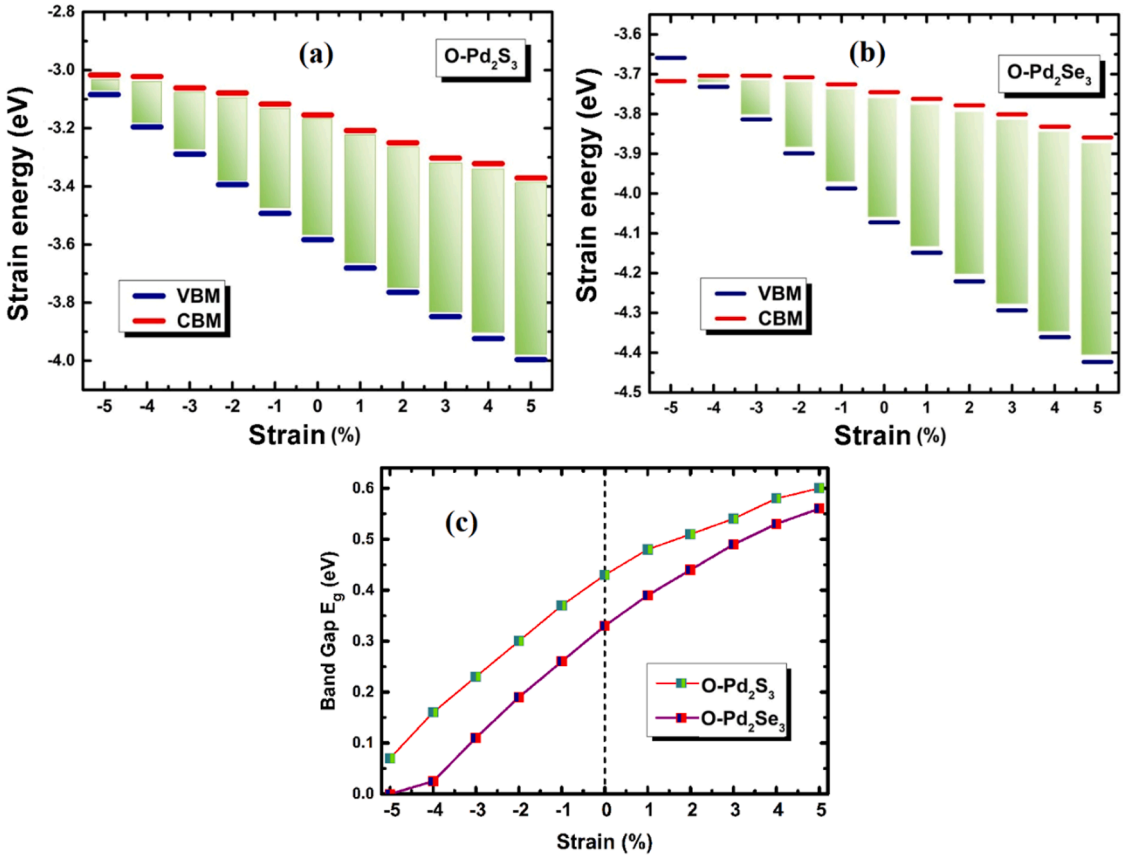

Fig. 3. The variation of the band edges of the CBM and VBM under biaxial strain (%) for (a) O-Pd_2S_3 and (b) O-Pd_2Se_3 (c) Calculated band gaps of the O-Pd_2Q_3 monolayers as a function of the biaxial strain.

3. Results and discussion

3.1. Structural and electronic properties of O-Pd_2Q_3 (Q = S, Se) monolayers

After full optimization, the atomic structure of the orthorhombic Pd_2Q_3 (Q=S, Se) monolayered structures is illustrated in Fig. 1 (a, b). They both consist of a layer of Pd atoms, having square-planar coordination, sandwiched between two layers of the chalcogen S(Se) atoms. The O-Pd_2Q_3 systems are built from four Pd and six Q (S, Se) atoms in the unit cell, adopting a lace-like geometry. As presented in Fig. 1 (c, d), an accumulation and depletion of charges between Pd and (S, Se) atoms occur in the form of a differential charge density. More explicitly, the partial charge on the S atom is -0.187*e* and on the Pd is 0.131*e*, implying that sulfur is a charge acceptor, and Pd is a charge donor. Similarly, for the O-Pd_2Se_3 monolayer, the atomic charge on an Se (Pd) atom is -0.119*e* (0.071*e*). The total charge per unit cell is, therefore -0.59*e* for O-Pd_2S_3 and -0.43*e* for O-Pd_2Se_3.

The relaxed structural parameters, such as the lattice constant, bond-lengths *d*, and vertical height *h* are collected in Table I. Our calculated lattice parameters *a* (*b*) of O-Pd_2S_3 and O-Pd_2Se_3 monolayers are 5.85 (5.40) Å and 6.15 (6.11) Å, which are in fine agreement with the theoretical results of Xiong et al. [20]. The atomic distances and vertical height values are also in good agreement with those of reference [20].

We evaluated the energetic stability of these O-Pd_2Q_3 monolayers by computing their cohesive energy (E_{coh}), determined as $E_{coh} = (E_{Pd2Q3} - \Sigma n_X E_X)/ N$, where E_{Pd2Q3} and N denote the total energy and the total number of atoms in a Pd_2Q_3 (Q = S, Se) unit cell respectively. n_X represents the number of atoms of each element X, and E_X is its energy (as an isolated atom). Our results demonstrate that the cohesive energy for O-Pd_2S_3 is -5.99 eV/atom and -5.88 eV/atom for O-Pd_2Se_3. These values are larger than those of 2D silicene (-3.71 eV/atom) [33] and phosphorene (-3.61 eV/atom) [34]. We have further verified the dynamical stability of the materials by computing their phonon dispersive curves. As shown in Fig. 2 (a, c), no imaginary phonon modes are present in the phonon spectrum for both monolayers, indicating that they can be practically utilized. We also realize that some of the optical modes -including the highest ones- are quasi-flat, which results in lower values of the group velocity compared to the other optical modes and/or the acoustical modes. In O-Pd_2S_3(O-Pd_2Se_3), the average group velocity for acoustical modes is found to be 2.29km/s (2.39km/s), while that for the remaining 27 optical modes evaluates to 0.42km/s (0.48km/s).

Investigating the mechanical stability of the 2D structures in question, we have deduced the Bulk modulus B (N/m) and Young's Y (N/m) modulus of the materials under biaxial and uniaxial strain, by determining how the total energy changes with strain (please refer to ESI (Fig. S1 and S2, ESI†)). The applied strain ε(%) is taken within the interval -5% ≤ ε ≤ +5% in steps of 0.5%. The obtained bulk modulii of O-Pd_2S_3 and O-Pd_2Se_3 are 49.57 N/m and 32.97 N/m, respectively. These results suggest that both monolayers are much stiffer and are resistant to deformation, better than 2D arsenic (~ 25.78 N/m) [35], antimony (~ 21.88 N/m) [36] and PdS_2 (~ 30.22 N/m) [3] monolayers. The calculated Young's modulus along the *x* (*y*) direction are 67.73 (65.90 N/m) and 46.44 (49.35 N/m), for O-Pd_2S_3 and O-Pd_2Se_3 respectively. Other than being slightly anisotropic, the structures have a lower Young's modulus compared to 2D MoS_2 (~ 125 N/m) [37]. This strongly points to the fact that the O-Pd_2Q_3 materials are more suited to build flexible nanodevices. The flexibility of the O-Pd_2Se_3 monolayer is reported up to a 53% critical strain by Peng et al. [38].

The pictorial representation of the electronic band structure and total and projected density of states/eV of the O-Pd_2Q_3 monolayers are shown in Fig. 2 (b, d). At the PBE level, the electronic band structure is

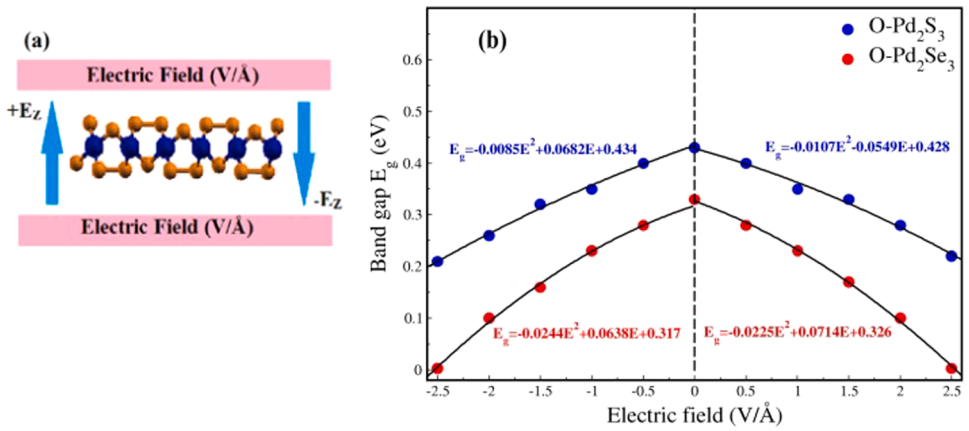

Fig. 4. (a) Schematic representation of the applied external electric field on a O-Pd_2Q_3 monolayer (b) Electronic band gap variation with the external electric field, showing the parabolic fitting (continuous curves) for positive and negative values of $\vec{E}$.

calculated along the high symmetry Γ-X-S-Y-Γ path in the first Brillouin zone. It is observed that both monolayers have a semiconducting behavior with fundamental indirect band gaps of 0.43 eV and 0.33 eV for O-Pd_2S_3 and O-Pd_2Se_3, respectively. The conduction band minima (CBM) are located at the S point in O-Pd_2S_3 and along the S-Y path in O-Pd_2Se_3. On the other hand, the valence band maxima (VBM) are situated at the Γ point. The obtained band gaps are quite comparable with other available theoretical measurements [20,22,23]. Although they are known to produce more accurate results and exhibit fewer errors in the positioning of the eigenvalue at the band extrema with respect to the average electrostatic potential, we have not computed the bandgap at the hybrid HSE06 (Heyd-Scuseria-Ernzerhof) level [39] because they are very time consuming and require high computational power.

The total (TDOS) and partial density of states (PDOS) are shown in Fig. 2 (b, d). It is found that the TDOS of both materials is mainly contributed by the '*d*' orbitals of Pd, and the '*p*' orbitals of the Q (Q= S, Se) atoms. More specifically, the PDOS of the O-Pd_2Q_3 monolayers suggests that the top of the valence band (VB) and the bottom of the conduction band (CB) are dominated by Pd-*4d* and S-*3p* (Se-*4p*) orbitals.

3.2. Carrier mobility of the O-Pd_2Q_3 (Q = S, Se) monolayers

Mechanical strain is one of the simplest and most efficacious ways to modify the electronic states of a material. Here, we have applied a biaxial strain, and verified its effect on the edges of VBM and CBM in the electronic band structures of the O-Pd_2Q_3 monolayers. We have also investigated the transport properties in terms of the carrier mobility for the various strengths of the biaxial strain, as this is a very important aspect of the performance of field effect transistors (FETs).

We define compressive and tensile strain values, in percentage form, according [40] to $\varepsilon = [(a\text{-}a_0)/a_0] \times 100\%$. The influence of the applied strains on the band edge positions of the CBM and VBM of the materials is depicted in Fig. 3 (a-b). We note that, under tensile strain, the band gap of both systems gradually increases. Contrarily, it decreases, in the case of compressive strain.

Fig. 3 (c) shows the band gap variation under compressive (-ε%) and tensile strain (+ ε%) within the range of -5% $\leq\varepsilon\leq$ +5%. Upon increasing the compressive strain (-ε%) in O-Pd_2S_3, its band gap goes down reaching a value of 0.07 eV at -5%, which is very close to becoming a metal. In contrast, if we keep increasing the tensile strain, the band gap continuously opens up and reaches a value of 0.6 eV at +5%. This behavior is best explained by the drastic decrease of the VBM edge energies, as observed in Fig. 3(a). The story is a bit different in O-Pd_2Se_3; upon increasing the compressive strain, the band gap also decreases but, in this case, the remarkable resistive phase transition is seen at -5%, where O-Pd_2Se_3 is converted from a semiconductor to a metal. This arises due to the crossing of the VBM and the CBM at the fermi level as displayed in Fig. 3(b). Similar to the case of O-Pd_2S_3, increasing the tensile strain causes the band gap to rise further, reaching a value of 0.56 eV at ε =+5%. These results imply that both monolayers can be tuned, according to one's needs, making them plausible candidates for modeling nanodevices.

Based on these intriguing properties of the O-Pd_2Q_3 monolayers, we further calculated the room temperature carrier mobility under biaxial strain. Three ingredients are needed to evaluate μ_{2D}, namely the deformation potential E_1 (eV) (obtained from the deformation potential (DP) theory [27]), the effective mass m^*, and the two-dimensional stiffness constant C_{2D}, the values of which are summarized in Table 2. The obtained effective mass of electrons and holes for O-Pd_2S_3 (O-Pd_2Se_3) are $0.79m_e$ ($0.78m_e$) and $1.44m_e$ ($1.35m_e$), respectively, m_e being the mass of a free electron. The stiffness constant C_{2D} of O-Pd_2Q_3 is 198.26 J m^{-2} for O-Pd_2S_3, and 133.30 J m^{-2} for O-Pd_2Se_3. Furthermore, the computed deformation potential E_1 of O-Pd_2S_3 is 2.42 eV for electrons (e) and -2.75 eV for holes (*h*), with electron and hole mobilities of the order of 766.09 $cm^2\ V^{-1}\ s^{-1}$ and ~ 596.91 $cm^2\ V^{-1}\ s^{-1}$, respectively. These values are quite larger than those registered for a boron nitride (BN) nanosheet (500 $cm^2\ V^{-1}\ s^{-1}$) [41], and a phosphorene monolayer (286 $cm^2\ V^{-1}\ s^{-1}$) [42]. In the case of O-Pd_2Se_3, the value of E_1 is 3.15 eV for electrons and -3.11 eV for holes. The achieved hole mobility is ~ 105.73 $cm^2\ V^{-1}\ s^{-1}$, which is 1.16 larger than that of the electrons (~ 91.45 $cm^2\ V^{-1}\ s^{-1}$). These are significantly higher than those reported for transition metal dichalcogenides (TMDCs) such as MoS_2 and WSe_2 (~ 100 $cm^2\ V^{-1}\ s^{-1}$) [37]. In conclusion, we can affirm that both monolayers have high carrier mobility along the biaxial strain, and thus could be further exploited to model electronic devices. The fact that $\mu_{2D,e}$ ($\mu_{2D,h}$) for O-Pd_2S_3 are almost 8 (6) times larger than those for O-Pd_2Se_3, results in larger electron and hole lifetimes (as illustrated in Table 2). Additionally, these values are larger than those obtained, along the x and y directions, by Naghavi et al. [22].

3.3. Influence of external electric fields on the O-Pd_2Q_3 (Q = S, Se) monolayers

Another approach to tune the band gap of the O-Pd_2Q_3 monolayers would be through the exertion of an external electric field $\vec{E}$ (V/Å) along the ±z-axis direction, as schematized in Fig. 4(a). Here, the magnitude of $\vec{E}$ is varied from -2.5 V/Å *to* +2.5 V/Å in steps of 0.5 V/Å. The variation of the bandgap with $\vec{E}$ is displayed in Fig. 4(b).

As observed in Fig. 4(b), we have included a separate parabolic fitting (shown as black continuous curves) for positive and negative electric fields. Equations in blue refer to the O-Pd_2S_3 system, while those

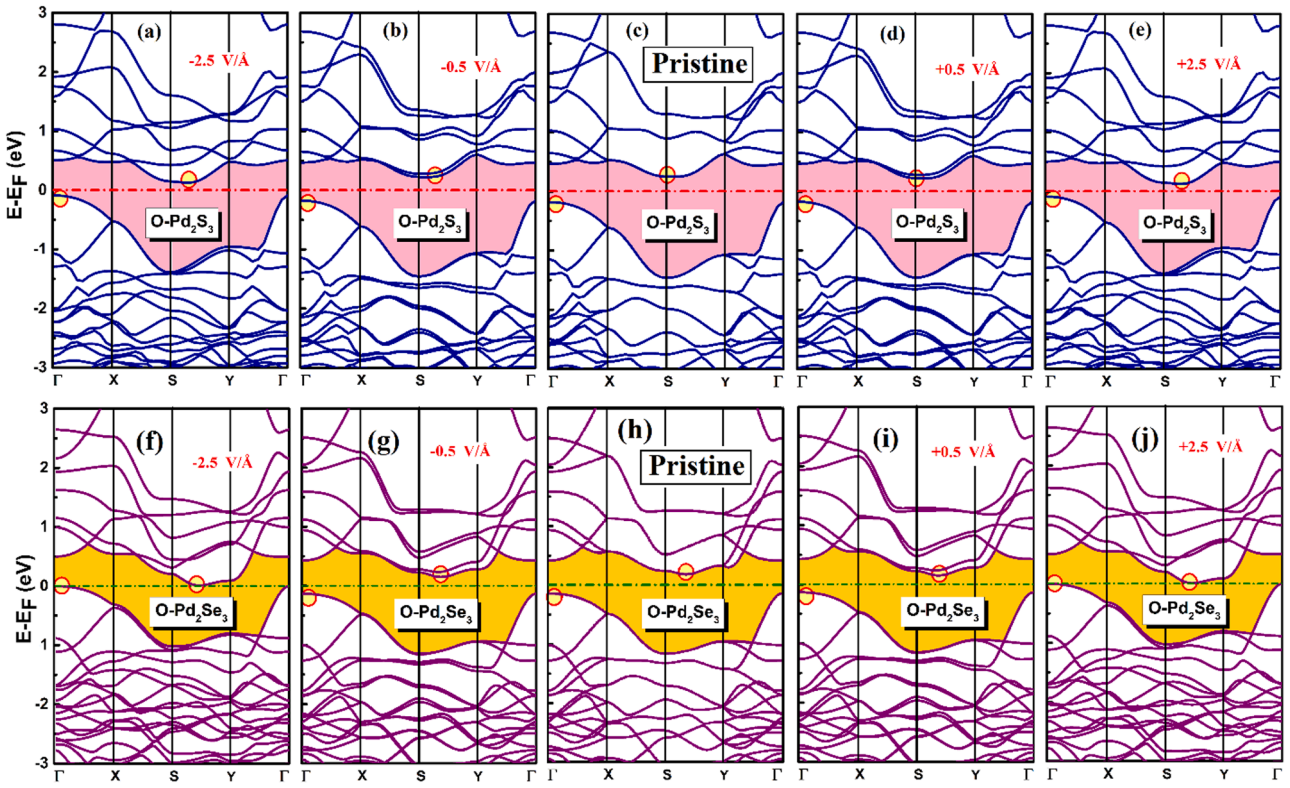

Fig. 5. Band structures under the applied external electric field (a-e) for the O-Pd_2S_3 and (f-j) for the O-Pd_2Se_3 monolayers. The red circles mark the VBM and CBM positions for each case.

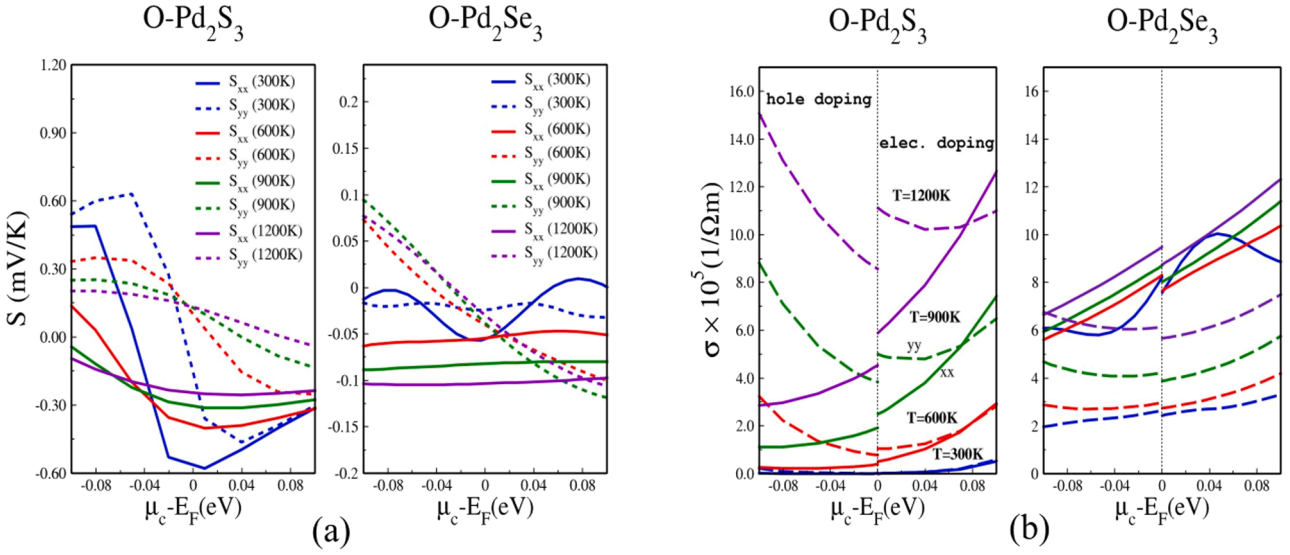

Fig. 6. (a) The Seebeck coefficient, in mV/K, and (b) the electronic conductivity (σ) in 1/(Ωm) for the O-Pd_2S_3 and O-Pd_2Se_3 monolayers within a ±0.1eV energy range. The electron and hole doping regimes –separated by the vertical 0eV line- are also shown.

in red correspond to the O-Pd_2Se_3 monolayer. The band gap of the O-Pd_2Q_3 monolayer decreases for positive (parallel) and negative (anti-parallel) values of $\vec{E}$. In particular, the band gap, for the O-Pd_2Se_3 monolayer, ceases to exist at ±2.5 V/Å, marking the beginning of a semiconductor-metal transition; this is due to the shifting of the CBM towards the Fermi level. Contrary to O-Pd_2Se_3, the O-Pd_2S_3 monolayer remains an indirect band gap semiconductor; more specifically, when $|\vec{E}|$= ±2.5 V/Å, the band gap energy in O-Pd_2S_3 decreases to ~51% of its initial value (when the field was absent). Upon increasing the intensity of the external electric field along the ±z direction, the CBM of both monolayers are slightly shifted to the right side, from the S symmetry point, with no significant changes in the nature of the band structure (except for the electronic band gap values) being detected. Very small changes are seen in the valence bands, as illustrated in Fig. 5 (f, j). Such type of behavior is also manifest in several semiconducting monolayers [43–47].

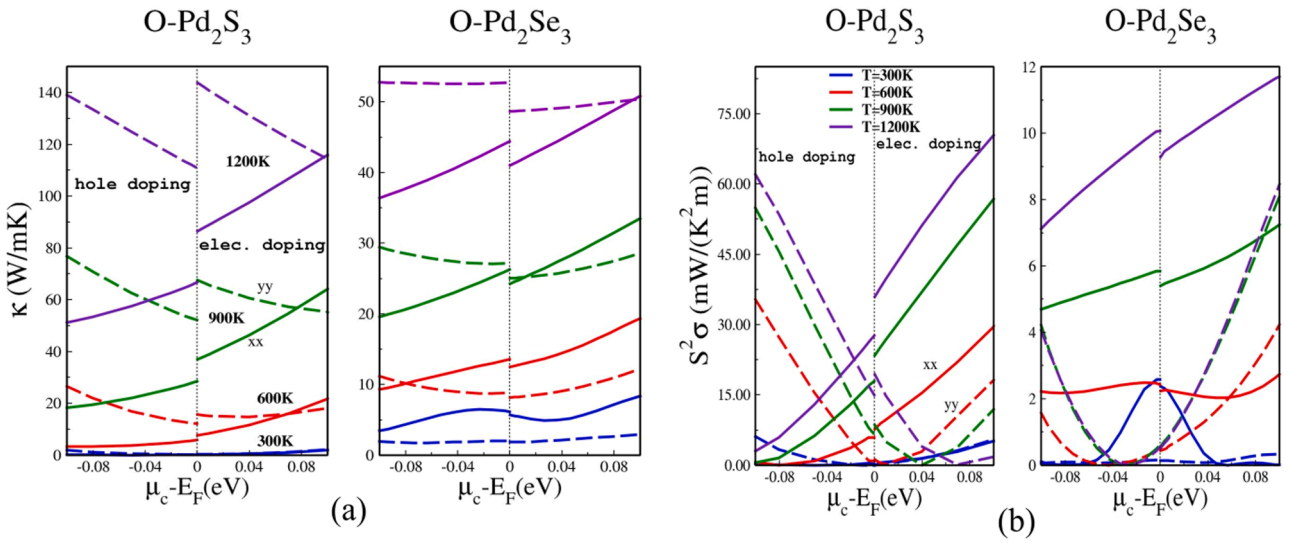

FIG. 7. Same as in Fig. 6 but for κ (in W/(m.K)) and the PF (in mW/(m.K^2)).

3.4. *Thermal properties of the O-Pd_2Q_3 (Q = S, Se) monolayers*

First of all, we will shine light on how each of the Seebeck coefficient (S), the electronic conductivity (σ), and the electronic thermal conductivity (κ) change with μ_c at different temperatures, namely T=300K, 600K, 900K, and 1200K. Based on the rigid band approximation (RBA) [48,49], shifting the Fermi energy towards the conduction bands mimics electron doping, while shifting it towards the valence bands corresponds to hole doping. The shift cannot however be large since this would imply heavy doping, the limit at which the RBA breaks down. To be realistic, and since we are chiefly interested in the area very close to the Fermi level, the variation of μ_c will be examined within a ±100meV energy interval. This turns out to be a judiciously good approximation and has been able to successfully define the transport coefficients of many materials [50,51]. The results can be found in Figs. 6 and 7, where the "xx" and "yy" subscripts will refer to the x and y planar directions respectively.

From now on, the values of the thermoelectric properties are reported near E_F. The lowest energy values at which these quantities are evaluated are at ±0.1meV from μ_c=E_F. Starting with O-Pd_2S_3, we notice that along the x-direction, the Seebeck coefficient S (Fig. 6(a)) increases with T, registering values of -0.59mV/K, -0.39mV/K, -0.30mV/K, and -0.25mV/K at 300, 600, 900, and 1200K respectively. Along the y direction, we obtain -0.17mV/K at 300K, 0.10mV/K at 600K, 0.12mV/K at 900K and 0.13mV/K at 1200K. It is clear that S is anisotropic, and thus does not have the same values along the x and y directions. Regarding the O-Pd_2Se_3 system (Fig. 6(b)), S registers -0.06mV/K at 300K and -0.1mV/K at 1200K along the x-direction. Along the y-direction, it starts from the value -0.02mV/K at 300K, -0.04mV/K at 900K, and then goes to -0.03mV/K at 1200K. It should be noted that the reported values for the Seebeck coefficient are the same for μ_c=E_F+0.1meV and E_F-0.1meV, and therefore it is continuously defined at μ_c=E_F; this is attributed to the fact that S is independent of the electronic lifetime (τ).

Due to their dependence on the electronic lifetime, which is different for electrons and holes, σ and κ are expected to be different for the electron (corresponding to E>E_F) and hole (corresponding to E<E_F)

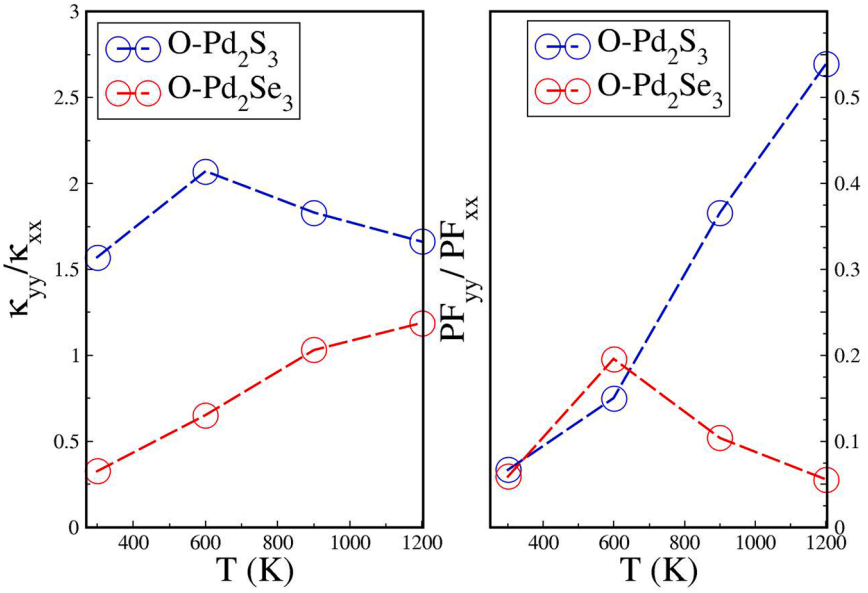

FIG. 8. The ratios of the electronic thermal conductivity κ and the power factor ($S^2\sigma$) along the x and y directions for the O-Pd_2X_3 monolayers, at μ=E_F. The dashed lines only serve as a guide to the eye.

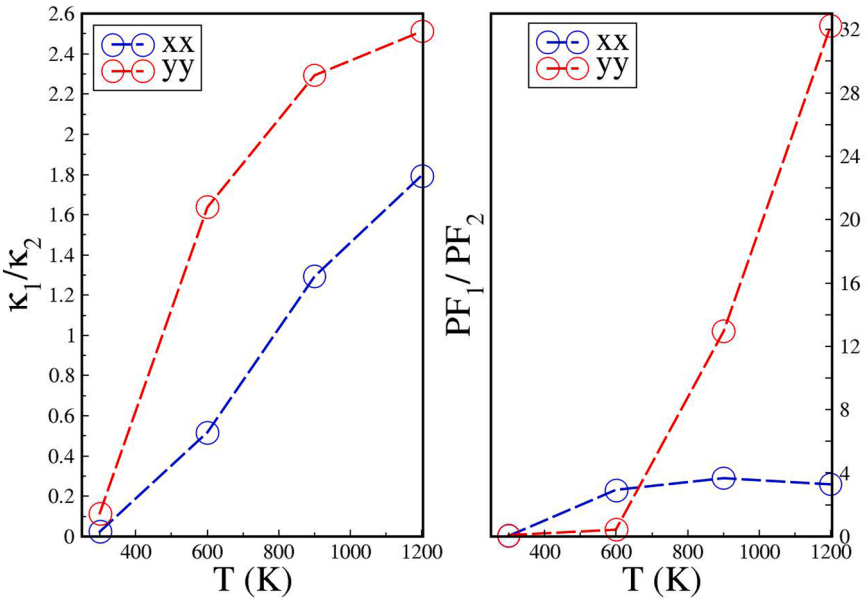

FIG. 9. The ratios of the electronic thermal conductivity κ and the power factor ($S^2\sigma$) of the materials along a specific x (y) direction at μ=E_F. The subscripts "1" and "2" correspond to O-Pd_2S_3 and O-Pd_2Se_3 respectively. The dashed lines only serve as a guide to the eye.

doping, at energies very close to E_F. The electronic conductivity also shows an anisotropic behavior (Fig. 6 (b)). At a constant temperature T, the ''xx'' and ''yy'' components are not equal in either case of electron or hole doping. In general, it appears that the conductivities along the y direction are higher than those along the x-direction in O-Pd_2S_3. This situation is reversed for the O-Pd_2Se_3 monolayers, where it is evident that the electronic conductivities along the x-direction are larger. Moreover, for O-Pd_2S_3 monolayers and looking at either the "xx" (or "yy") component, the difference in σ at μ_c-E_F =0.1meV and -0.1meV does not exceed 27% for T ≥600K. Although this pattern is also seen in O-Pd_2Se_3, the dissimilarity is much smaller (~8%), probably due to the comparable electron and hole lifetimes for this material.

As T increases, the thermal electronic conductivity (κ) increases as well. Overall, the values are larger for O-Pd_2S_3 monolayers (Fig. 7(a)). In this system, κ_{yy} seems to be larger than κ_{xx}, along most of the energy range considered, and for both electron and hole doping. In contrast, for O-Pd_2Se_3, $\kappa_{xx}>\kappa_{yy}$ for T=300 and 600K, and for the case of electron doping at T=900K. Otherwise, κ_{yy} is larger.

Another principal quantity that can be obtained from S and σ is the power factor (PF), given by $S^2\sigma$. It is an indicator of the usefulness of a material in thermoelectric generators or coolers. The higher the PF, the more energy the materials generate, due to a temperature difference. The change in the PF with respect to (μ_c–E_F) is depicted in Fig. 7 (b). As T increases, PF increases as well in both structures. On average and as was realized for the case of κ, the PF for O-Pd_2S_3 extends to higher values. While $PF_{yy} > PF_{xx}$ in the case of hole doping (except for energies up to ±0.02eV from E_F), $PF_{yy} < PF_{xx}$ for electron doping. For T≥600K and the case of hole doping, $PF_{yy} < PF_{xx}$ in the O-Pd_2Se_3 monolayers. This is also true for T≥900K in the case of electron doping. The maximum values of S, σ, κ, and the PF could be easily extracted from Figs. 6 and 7. Detailed values of all of these thermoelectric physical quantities at μ_c-E_F=±0.1meV at the different temperatures are found in ESI (Tables S1 and S2, ESI†).

Once more, the values of these quantities are not identical as we approach E_F from both sides. The deviations do not exceed 27% for O-Pd_2S_3 and 8% for O-Pd_2Se_3. Nevertheless, this makes the functions ill-defined at μ_c=E_F. We can resolve this issue by taking the average of the two results in the neighborhood of the Fermi level, for each (x or y) direction. As an example, for the case of O-Pd_2S_3, we have at T=600K, σ_{xx}(h)=3.87 × 10^4 1/(Ωm) and σ_{yy}(e)=5.08 × 10^4 1/(Ωm). The reported value at μ_c=E_F would then be (σ_{xx} (h)+σ_{xx} (e))/2, that is 4.47 × 10^4 1/(Ωm). Fig. 8 graphically demonstrates the ratios κ_{yy}/κ_{xx}, and PF_{yy}/PF_{xx} for both structures at μ_c=E_F. At any T, $\kappa_{yy}/\kappa_{xx} \geq 1.5$ for O-Pd_2S_3. Contrarily, for O-Pd_2Se_3, $\kappa_{yy}/\kappa_{xx} < 1$ except at 1200K, where it registers a value of. 1.18 At T=900K, this material exhibits an isotropic behavior such that $\kappa_{xx} \sim \kappa_{yy}$. On the other hand, anisotropy in PF is such that $PF_{yy}/PF_{xx} < 1$ for both materials at any T, suggesting that properties along the x-directions are to be exploited for thermoelectric applications.

A complementary figure (Fig. 9) compares κ and PF of the O-Pd_2Q_3 materials along a specific direction. Along the x-direction, O-Pd_2Se_3 shows a larger thermal electronic conductivity for T ≤600K. For T ≥900K, κ for the O- Pd_2S_3 monolayers is larger along both x and y directions. Similarly, O-Pd_2S_3 monolayers depict excellent thermoelectric performance for T>600K. At 900K and along the y-direction, O-Pd_2S_3's power factor is ~ 13 times that of O-Pd_2Se_3. At 1200K, this value becomes ~ 32. At ambient temperatures, O-Pd_2Se_3 constitutes a better choice, for its power factor is almost 18 (16) times that of O-Pd_2S_3 along the x (y)-direction.

Compared to other related 2D materials, the average κ (T=300K) for 1T PdS_2 is 0.11 W/(m K) [52]; the analogous value for O-Pd_2S_3 is slightly higher (0.18 W/(m K)). For 1T $PdSe_2$, κ (T=300K) ~1.4 × 10^{-3} W/(m K), which is negligible, compared to the value we acquired for O-Pd_2Se_3 (3.91 W/(m K)). Similarly, the average power factors for 1T PdS_2 (3.5 × 10^{-4} mW/(m K^2)) is ~ 200 times smaller than the one estimated for O-Pd_2S_3 (0.072 mW/(m K^2)). Furthermore, the average reported PF for 1T $PdSe_2$ (4.4 × 10^{-6} mW/(m K^2)) at 300K is negligible, compared to what is obtained for O-Pd_2Se_3(1.31 mW/(m K^2)); the latter value is also slightly larger than that depicted for pentagonal $PdSe_2$ (1.25 mW/(m K^2)) [53].

Knowledge of the group velocities for each of the three acoustical modes allows the evaluation of the minimum lattice thermal conductivity κ_L^{min} at the limit of high T. Based on Cahill's model [54], the individual phonons vibrate independently of one another, with the lifetime obtained as half of the period of vibration of each mode. Besides, the optical group velocities (v_o) are smaller than the acoustical ones (v_a); namely, v_o/v_a =0.18 for O-Pd_2S_3 and 0.2 for O-Pd_2Se_3. These approximations permit us to define:

$$\kappa_L^{min} = \frac{k_B}{2.48} n^{2/3} \sum_{i=1}^{3} v_i \quad (4)$$

Table 1
Lattice parameter (Å), Pd-Q_1(Q_2) and Q_1-Q_3 bond lenghts *d* (Å), height *h* (Å) and the cohesive energy E_{coh} (eV/atom) of the O-Pd_2Q_3 monolayers. Comparison with other results in the literature is included.

O-Pd_2Q_3 (Q=S, Se)		$d_{Pd\text{-}Q2}$ (Å)	$d_{Pd\text{-}Q1}$ (Å)	$d_{Q2\text{-}Q3}$ (Å)	h (Å)	Lattice parameter (Å)	E_{coh} (eV/atom)
O-Pd_2S_3	Present work	2.34	2.44	2.15	3.59	a= 5.85, b= 5.40	-5.99
	Other	2.34 [20]	2.42 [20]	–	3.58 [20]	a= 5.90, b= 5.77 [20]	
O-Pd_2Se_3	Present work	2.48	2.58	2.45	3.85	a=6.15, b= 6.09	-5.88
	Other	2.45 [20]	2.53 [20]	2.40 [22]–	3.84 [20]	a=6.12, b=5.95 [22]	
						a= 6.12, b= 6.11 [20]	

Table 2
Predicted electron ($\mu_{2D,e}$) and hole mobility ($\mu_{2D,h}$), as well as the electron (τ_e) and hole (τ_h) lifetimes along the biaxial direction of the O-Pd_2Q_3 monolayers at 300 K. The ratio (R) of the mobilities is also displayed.

System	Carrier type	m^*/m_e	E_1 (eV)	C_{2D} (J m^{-2})	μ_{2D} (cm^2 V^{-1} s^{-1})	τ_e (τ_h)(fs)	$R = \mu_{2D,h} / \mu_{2D,e}$
O-Pd_2S_3	e	0.79	2.42	198.26	766.09	344	0.78
	h	0.78	-2.75	198.26	596.91	265	
O-Pd_2Se_3	e	1.44	3.15	133.30	91.45	74.9	1.16
	h	1.35	-3.11	133.30	105.73	81.3	

k_B is the Boltzmann constant, *n* is the number of atoms per volume of the unit cell, and v_i is the average group velocity of the flexural (ZA), transverse (TA), and longitudinal (LA) acoustical modes. Evaluating this expression, we obtain κ_L^{min}=0.207 W/(m.K) for both structures. This is expected since the average group velocities and the value of *n* of O-Pd_2S_3 and O-Pd_2Se_3 are close. By analyzing the results in Naghavi et al. [22] and considering the average acoustical group velocities along the "a" and "b" directions of O-Pd_2Se_3 (as depicted in Table 1 in [22]), Eq. (4) evaluates to 0.17 W/(m.K). This compares well to our result, with just an 18% difference.

4. Conclusions

In summary, DFT calculations have been employed to study the electronic, transport, and thermal properties of the O-Pd_2Q_3 (Q= S, Se) monolayers. A positive phonon spectrum is an indication of the dynamical stability of both materials. The measured electronic band gaps are 0.33 eV and 0.43 eV for O-Pd_2S_3 and O-Pd_2Se_3, respectively. The calculated carrier mobility of O-Pd_2S_3 is ~ 766.09 cm^2 V^{-1} s^{-1} for electrons and ~ 596.91 cm^2 V^{-1} s^{-1} for holes, which is comparably higher than those reported for TMDCs. Biaxial strains and external electric fields were applied to the O-Pd_2Q_3 monolayers, in an attempt to tune their electronic properties. We have realized that O-Pd_2Se_3 can be changed into a metal for a compressive strain of 5%, and electric field magnitudes of ±2.5 V/Å. Although the bandgap of O- Pd_2S_3 gets reduced upon the application of a compressive strain and electric fields, the structure remains a semiconductor. In fact, the exertion of an electric field is symmetrical, causing a reduction in the bandgap for both parallel and antiparallel directions, with almost the same amount. This is opposed to the effect of biaxial strain, which tends to reduce the bandgaps, when it is compressive and increases them when it is of a tensile nature.

The thermoelectric properties of the O-Pd_2S_3 and O-Pd_2Se_3 monolayers were also considered. We have computed the Seebeck coefficient, electronic and thermal electronic conductivity, as well as the power factor at ambient and higher temperatures for energies up to ±100meV from the Fermi level. These properties were evaluated using two different electronic lifetimes: one for holes for $E < E_F$, and another for electrons corresponding to $E > E_F$. For our undoped systems (that is at μ=EF), and at T=300K, the O-Pd_2Se_3 monolayers are characterized by electronic thermal conductivities of around 42 and 8.8 times larger than those obtained for O-Pd_2S_3 along the x and y directions, respectively. Such large values could contribute to the reduction of the figure of merit (ZT) of these materials. At that same temperature, their power factors are 18 (16) times larger along the x (y) direction. When T increases above 600K, the power factor of Pd_2S_3, along both directions, becomes the largest. Furthermore, these values are far greater than those stated for 1T PdS_2, 1T $PdSe_2$, and penta-$PdSe_2$ monolayers. Using the average group velocity of the three acoustical modes, the minimum lattice thermal conductivities at high temperatures were measured to be 0.207 W/(m.K) for both compounds. The unique electronic, transport and thermal properties of the O-Pd_2Q_3 monolayers discussed in this manuscript serve as an essential guide, based on which future thermoelectric nanodevices, of prominent performance, could be built.

Data availability

The data that support the finding of this study are available from the corresponding author(s) upon reasonable request.

Credit authorship contribution statement

Dhara Raval, Elie A. Moujaes, S.K.G and P.N.G studied the conception and designed the final approval of the version to be published. Dhara Raval and Elie A. Moujaes were associated with the DFT calculations. Dhara Raval, Elie. A. Moujaes, S.K.G, and P.N.G contributed to the improvement of the scientific content of the article. All authors reviewed the manuscript.

Declaration of Competing Interest

The authors declare that they have no known competing financial interests or personal relationships that could have appeared to influence the work reported in this paper.

Data Availability

No data was used for the research described in the article.

Acknowledgement

The computer facility developed under DST-FIST Level-I (No.SR/FST/PSI-097/2006 dated 20th December 2006 and No.SR/FST/PSI-198/2014 dated 21 November 2014) programmes of Department of Science and Technology, Government of India, New Delhi, India and support under DRS-SAP-I (No. F-530/10/DRS/2010 (SAP-I) dated November 2010 and No.F.530/17/DRS-II/2018 (SAP-I), dated 17th April 2018) of University Grants Commission, New Delhi, India are highly acknowledged. Dhara Raval is thankful for the project fellowship

under DRS-II-SAP (No.F.530/17/DRS-II/2018 (SAP-I), dated 17/04/2018) of University Grants Commission, New Delhi, India. S.K.G. would like to thank the Science and Engineering Research Board (SERB), India for the financial support (Grant no.: YSS/2015/001269).

Supplementary materials

Supplementary material associated with this article can be found, in the online version, at doi:10.1016/j.surfin.2022.102396.

References

[1] AK. Geim, KS. Novoselov, The rise of graphene, Nanosci. Technol. (2010) 11–19.
[2] AD. Oyedele, S. Yang, L. Liang, AA. Puretzky, K. Wang, J. Zhang, P. Yu, PR. Pudasaini, AW. Ghosh, Z. Liu, CM. Rouleau, PdSe$_2$: pentagonal two-dimensional layers with high air stability for electronics, J. Am. Chem. Soc. 139 (40) (2017) 14090–14097.
[3] D. Raval, SK. Gupta, PN. Gajjar, R. Ahuja, Strain modulating electronic band gaps and SQ efficiencies of semiconductor 2D PdQ2 (Q= S, Se) monolayer, Sci. Rep. 12 (1) (2022) 1–3.
[4] ES. Kadantsev, P. Hawrylak, Electronic structure of a single MoS2 monolayer, Solid State Commun. 152 (10) (2012) 909–913.
[5] B Babariya, D. Raval, SK. Gupta, PN. Gajjar, Modulation of band gap and optical response of layered MoX2 (X= S, Se, Te) for electronic and optoelectronic applications, Mater. Today Commun. 28 (2021), 102614.
[6] D. Muoi, NN. Hieu, HT. Phung, HV. Phuc, B. Amin, BD. Hoi, NV. Hieu, LC. Nhan, CV. Nguyen, PT. Le, Electronic properties of WS2 and WSe2 monolayers with biaxial strain: a first-principles study, Chem. Phys. 519 (2019) 69–73.
[7] S. Yang, C. Wang, H. Sahin, H. Chen, Y. Li, SS. Li, Suslu A, FM. Peeters, Q. Liu, J. Li, S. Tongay, Tuning the optical, magnetic, and electrical properties of ReSe2 by nanoscale strain engineering, Nano Lett. 15 (3) (2015) 1660–1666.
[8] J. Feng, X. Sun, L. Peng, C. Lin, S. Hu, J. Yang, Y. Xie, Metallic few-layered VS2 ultrathin nanosheets: high two-dimensional conductivity for in-plane supercapacitors, J. Am. Chem. Soc. 133 (44) (2011) 17832–17838.
[9] D. Raval, B. Babariya, SK. Gupta, PN. Gajjar, R. Ahuja, Ultrahigh carrier mobility and light-harvesting performance of 2D penta-PdX2 monolayer, J. Mat. Sci. 56 (5) (2021) 3846–3860.
[10] LH. Zeng, D. Wu, SH. Lin, C. Xie, HY. Yuan, W. Lu, SP. Lau, Y. Chai, LB. Luo, ZJ. Li, YH. Tsang, Controlled synthesis of 2D palladium diselenide for sensitive photodetector applications, Adv. Funct. Mater. 29 (1) (2019), 1806878.
[11] VB. Zala, RS. Shukla, PD. Bhuyan, SK. Gupta, PN. Gajjar, Highly selective and reversible 2D PtX2 (X= P, As) hazardous gas sensors: Ab-initio study, Appl. Surf. Sci. 563 (2021), 150391.
[12] SA. Svatek, C. Bueno-Blanco, DY. Lin, J. Kerfoot, C. Macias, MH. Zehender, I. Tobias, P. Garcia-Linares, T. Taniguchi, K. Watanabe, P. Beton, High open-circuit voltage in transition metal dichalcogenide solar cells, Nano Energy 79 (2021), 105427.
[13] T. Cao, G. Wang, W. Han, H. Ye, C. Zhu, J. Shi, Q. Niu, P. Tan, E. Wang, B. Liu, J. Feng, Valley-selective circular dichroism of monolayer molybdenum disulphide, Net. Commun. 3 (1) (2012) 1–5.
[14] S. Deng, L. Li, Y. Zhang, Strain modulated electronic, mechanical, and optical properties of the monolayer PdS2, PdSe2, and PtSe2 for tunable devices, ACS Appl. Nano Mater. 1 (4) (2018) 1932–1939.
[15] YS. Lan, XR. Chen, CE. Hu, Y. Cheng, QF. Chen, Penta-PdX$_2$ (X= S, Se, Te) monolayers: promising anisotropic thermoelectric materials, J. Mater. Chem. A 7 (18) (2019) 11134–11142.
[16] EA. Moujaes, WA. Diery, Optical properties and stability of new two-dimensional allotropes of PdS$_2$, PdSe$_2$ and PdSSe monolayers, Phys. E Low Dimens. Syst. Nanostruct. 128 (2021), 114611.
[17] D. Qin, P. Yan, G. Ding, X. Ge, H. Song, G. Gao, Monolayer PdSe2: a promising two-dimensional thermoelectric material, Sci. Rep. 8 (1) (2018) 1–8.
[18] M. Jakhar, J. Singh, A. Kumar, R. Pandey, First-principles study of the hexagonal T-phase PdSe2 monolayer and its application in solar cells, J. Phys. Chem. C 124 (49) (2020) 26565–26571.
[19] J. Lin, S. Zuluaga, P. Yu, Z. Liu, ST. Pantelides, K. Suenaga, Novel Pd$_2$Se$_3$ two-dimensional phase driven by interlayer fusion in layered PdSe2, Phys. Rev. Lett. 119 (1) (2017), 016101.
[20] W. Xiong, K. Huang, S. Yuan, The mechanical, electronic, and optical properties of two-dimensional transition metal chalcogenides MX$_2$ and M$_2$X$_3$ (M= Ni, Pd; X= S, Se, Te) with hexagonal and orthorhombic structures, J. Mat. Chem. C 7 (43) (2019) 13518–13525.
[21] SS. Naghavi, J. He, C. Wolverton, Crystal and electronic structures of palladium Sesquichalcogenides, Chem. Mater. 33 (7) (2021) 2298–2306.
[22] SS. Naghavi, J. He, Y. Xia, C. Wolverton, Pd2Se3 monolayer: a promising two-dimensional thermoelectric material with ultralow lattice thermal conductivity and high power factor, Chem. Mater. 30 (16) (2018) 5639–5647.
[23] X. Li, S. Zhang, Y. Guo, FQ. Wang, Q. Wang, Physical properties and photovoltaic application of semiconducting Pd2Se3 monolayer, Nanomaterials 8 (10) (2018) 832.
[24] J.M. Soler, E. Artacho, J.D. Gale, A. Garcia, J. Junquera, P. Ordejon, D. Sanchez-Portal, The SIESTA method for ab initio order-N materials simulation, J. Phys. Condens. Matter. 14 (11) (2002) 2745.
[25] J.P. Perdew, K. Burke, M. Ernzerhof, Generalized gradient approximation made simple, Phys. Rev. Lett. 2877 (18) (1996) 3865.
[26] X. Gonze, C. Lee, Dynamical matrices, Born effective charges, dielectric permittivity tensors, and interatomic force constants from density-functional perturbation theory, Phys. Rev. B 55 (16) (1997) 10355.
[27] J. Bardeen, W. Shockley, Deformation potential and mobilities in on-polar crystals, Phys. Rev. 80 (1) (1950) 72.
[28] J.M. Ziman, Electrons and Phonons: the Theory of Transport Phenomena in Solids, Oxford university press, 2001.
[29] W. Jones, N.H. March, Theoretical Solid State Physics, 35, Courier corporation, 1985.
[30] G. Pizzi, D. Volja, B. Kozinsky, M. Fornari, N. Marzari, BoltzWann: a code for the evaluation of thermoelectric and electronic transport properties with a maximally-localized Wannier functions basis, Compute. Phys. Commun. 185 (1) (2014) 422–429.
[31] P. Giannozzi, S. Baroni, N. Bonini, M. Calandra, R. Car, C. Cavazzoni, D. Ceresoli, GL. Chiarotti, M. Cococcioni, I. Dabo, A. Dal Corso, QUANTUM ESPRESSO: a modular and open-source software project for quantum simulations of materials, J. Phys. Condens. Matter 21 (39) (2009), 395502.
[32] G.H. Wannier, The structure of electronic excitation levels in insulating crystals, Phys. Rev. 52 (3) (1937) 191.
[33] B. Feng, Z. Ding, S. Meng, Y. Yao, X. He, P. Cheng, I. Chen, K. Wu, Evidence of silicene in honeycomb structures of silicon on Ag (111), Nano Lett. 12 (7) (2012) 3507–3511.
[34] H. Liu, AT. Neal, Z. Zhu, Z. Luo, X. Xu, D. Tomanek, PD. Ye, Phosphorene: an unexplored 2D semiconductor with a high hole mobility, ACS Nano 8 (4) (2014) 4033–4041.
[35] O. Akbari, R. Ansari, S. Rouhi, Mechanical properties of pristine and Fe, V and Ti doped arsenene: density functional theory calculation, Mater. Res. Express 5 (1) (2018), 015025.
[36] P. Aghdasi, R. Ansari, Structural and mechanical properties of Sb and SbX (X= H, F, Cl and Br) monolayers, Solid State Commun. 311 (2020), 113849.
[37] D. Cakir, FM. Peeters, C. Sevik, Mechanical and thermal properties of h-MX2 (M= Cr, Mo, W; X= O, S, Se, Te) monolayers: a comparative study, Appl. Phys. Lett. 104 (20) (2014), 203110.
[38] P. Lv, G. Tang, C. Yang, J. Deng, Y. Liu, X. Wang, X. X. Wang, J. Hong, High Curie temperature half metallic 2D M2Se3 (M= Co, Ni, and Pd) monolayers with superior mechanical flexibility, arXiv preprint, 1805.07538 (2018).
[39] K. Hummer, J. Harl, G. Kresse, Heyd-Scuseria-Ernzerhof hybrid functional for calculating the lattice dynamics of semiconductors, Phys. Rev. B 80 (11) (2009), 115205.
[40] DM. Hoat, S. Amirian, H. Alborznia, A. Laref, AH. Reshak, M. Naseri, Strain effect on the electronic and optical properties of 2D Tetrahexcarbon: a DFT-based study, Indian J. Phys. 95 (11) (2021) 2365–2373.
[41] S. Bruzzone, G. Fiori, Ab-initio simulations of deformation potentials and electron mobility in chemically modified graphene and two-dimensional hexagonal boron-nitride, Appl. Phys. Lett. 99 (22) (2011), 222108.
[42] Y. Xu, G. Liu, G. Zhao, J. Yang, Tuning the mechanical and electronic properties and carrier mobility of phosphorene via family atom doping: a first-principles study, J. Mater. Chem. C 8 (42) (2020) 14902–14909.
[43] DM. Hoat, TV. Vu, MM. Obeid, HR. Jappor, Tuning the electronic structure of 2D materials by strain and external electric field: case of GeI2 monolayer, Chem. Phys. 527 (2019), 110499.
[44] XP. Wang, XB. Li, NK. Chen, JH. Zhao, QD. Chen, HB. Sun, Electric field analyses on monolayer semiconductors: the example of InSe, Phys. Chem. Chem. Phys. 20 (10) (2018) 6945–6950.
[45] DD Vo, TV Vu, TH Nguyen, NN Hieu, HV Phuc, NT Binh, M Idrees, B Amin, CV. Nguyen, Effects of electric field and strain engineering on the electronic properties, band alignment and enhanced optical properties of ZnO/Janus ZrSSe heterostructures, RSC Adv. 10 (17) (2020) 9824–9832.
[46] L Pan, B Zou, LJ. Shi, Electric field modulation of the band gap, dielectric constant, and polarizability in SnS atomically thin layers, Phys. Lett. A 380 (27-28) (2016) 2227–2232.
[47] J Wu, Y Yang, H Gao, Y Qi, J Zhang, Z Qiao, W. Ren, Electric field effect of GaAs monolayer from first principles, AIP Adv. 7 (3) (2017), 035218.
[48] GK. Madsen, Automatic search for new thermoelectric materials: the case of LiZnSb, J. Am. Chem. Soc. 128 (37) (2006) 12140–12146.
[49] J. Yang, H. Li, T. Wu, W. Zhang, L. Chen, J. Yang, Evaluation of half-Heusler compounds as thermoelectric materials based on the calculated electric transport properties, Adv. Funct. Mater. 18 (19) (2008) 2880–2888.
[50] H. Gzyl, Integration of the boltzmann equation in the relaxation time approximation, J. Stat. Phys. 29 (3) (1982) 617–622.
[51] T.J. Scheidemantel, C. Ambrosch-Draxl, T. Thonhauser, J.V. Badding, J.O. Sofo, Transport coefficients from first-principles calculations, Phys. Rev. B. 68 (12) (2003), 125210.
[52] E.A. Moujaes, W.A. Diery, Thermoelectric properties of 1 T monolayer pristine and Janus Pd dichalcogenides, J. Phys. 31 (45) (2019), 455502.
[53] D. Qin, P. Yan, G. Ding, X. Ge, H. Song, G. Gao, Monolayer PdSe2: a promising two-dimensional thermoelectric material, Sci. Rep. 8 (1) (2018) 1–8.
[54] D.G. Cahill, S.K. Watson, R.O. Pohl, Phys. Rev. B 46 (1992) 6131–6140.